Speckle statistics in a chaotic multimode fiber

Valérie Doya, Olivier Legrand, and Fabrice Mortessagne

Laboratoire de Physique de la Matière Condensée, CNRS UMR 6622, Université de Nice Sophia-Antipolis, 06108 Nice, France

Christian Miniatura

Laboratoire Ondes et Désordre, CNRS FRE 2302, 1361 Route des Lucioles, Sophia-Antipolis, 06560 Valbonne, France

Wave chaos is devoted to the study of wave motion when the geometrical limit of rays is chaotic. Imprints of ray chaos may be found either in spectral and spatial properties of modes or in spatio-temporal evolution of wave packets. In this paper, we present a thorough experimental and theoretical analysis of field statistics for light propagating in a multimode fiber with a noncircular cross section. This optical fiber serves as a powerful tool to image waves in a system where light rays exhibit a chaotic dynamics. We show that, in the speckle regime, the experimentally measured statistical properties of intensity patterns are well accounted for by a "random Gaussian" hypothesis. A comparison is also made in the case of regular ray motion by using a circular optical fiber. Possible extensions and applications of the tools and concepts of wave chaos are mentioned in modern communication technology.

PACS number(s): 05.45.Mt, 42.81.−i

I. INTRODUCTION

After three decades of studies in the field of *quantum chaos*, the nature of quantum eigenstates of systems whose classical limit is chaotic is still an active subject of research. In classical Hamiltonian dynamics, chaos is explained in terms of exponential instability of trajectories with respect to initial conditions, leading to mixing and ergodicity. Thus, the application of probability theory to these deterministic systems is justified [1]. It is crucial to realize that asymptotic (long-time) limits of dynamical averages are essential in classical ergodic theory. In contrast, bounded classically chaotic quantum systems show different behaviors since, their frequency spectrum being discrete, all phase-space information is essentially obtained after a finite amount of time. This conflicting situation reveals the subtle and singular nature of the semiclassical limit (boldly implemented as the famous "$\hbar \to 0$" limit) whose understanding is precisely the subject of quantum chaos. In this limit, wave functions are uniformly distributed over the whole available phase space, which is ergodically explored by the classical trajectories, thus locally resulting in a random superposition of plane waves. Tracking fingerprints of classical phase-space structures in quantum properties (distribution of eigenfrequencies, statistical properties of eigenmodes, Green's functions, and time evolution) led to major advances in the field, such as random matrix theory, and periodic orbit theory, dynamical localization [2]. In fact, these advances rapidly proved to be relevant for other wave systems sharing close analogies with quantum systems (e.g., microwave or acoustic systems), giving rise to *wave chaos*. For these systems, the goal is to understand the fate of interference in the geometrical limit (wavelength $\lambda \to 0$) when the ray motion is chaotic. Connections were also found with disordered systems [3]. Wave and quantum chaos are thus now well documented topics [2,4,5] covering a wide variety of physical systems, such as complex atomic nuclei [6], Rydberg atoms [7], electrons in quantum dots [8], cold atoms [9], surface waves [10], elastodynamics [11], acoustics [12], microwaves [13], and optical cavities [14]. Despite their interesting potentialities [15], wave chaos experiments with visible light, in particular in optical fibers, have been largely underestimated. Indeed, the huge advantage of light in optical fibers resides in the fact that it can be most easily imaged, thus enabling one to achieve very precise measurements of intensity patterns. Recently, using a chaotic optical fiber with a D-shaped transverse section, we have observed and analyzed scarred patterns [16]. While spectacular, this behavior is exceptional in such chaotic optical fibers, and a random field is more generally obtained. The differences between these behaviors can be evidenced through an analysis of the field in terms of spatial statistics and correlations. The aim of the present paper is to provide the first experimental characterization of wave intensity in multimode fibers in the speckle regime, together with a theoretical analysis in terms of wave chaos.

This paper is organized as follows. In Sec. II, we present a theoretical approach based on a modal decomposition to describe light propagation along a multimode fiber. To establish an analogy with quantum systems, we introduce the paraxial approximation, which we show to be valid in the system we consider. In Sec. III, we start from a Hamiltonian formalism for wave propagation to briefly describe the geometrical limit of rays and introduce the concept of chaotic billiards relevant to our study. Then semiclassical arguments are briefly reviewed and used to predict Gaussian statistics of guided modes. A brief mention of periodic orbit theory is made to illustrate the close connection between modes and periodic ray motion. In Sec. IV, our experiment is described, starting with the fabrication of a specially designed multimode fiber. The experimental setup is then presented, followed by an analysis of the measurements of wave intensity. We show the relevance of a Gaussian analysis for a wave pattern resulting from the superposition of ergodic guided modes. A special emphasis is placed on spatial correlations of the near-field using the information contained in the far-field intensity pattern. We cannot conclude without mention-
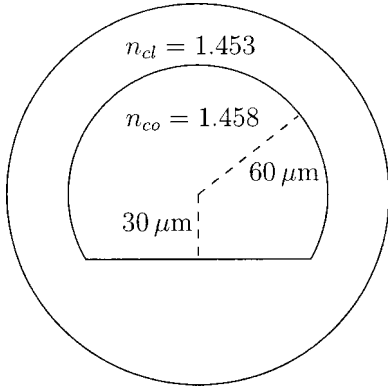
FIG. 1. Sketch of the transverse section of the multimode fiber studied in the paper. The cladding of the actual fiber is thicker than shown here.

ing that, in the current context of rapidly growing optical communications, the understanding and fine control of complex wave propagation in multimode fibers will constitute an indispensable issue in future transmission systems.

II. THE MODEL FOR PROPAGATION ALONG THE FIBER

We postpone to Sec. IV, dedicated to experimental results, the details of fabrication of the fiber we use. Here, we simply give those of its characteristics which justify the approximations of our model. We use a highly multimode step-index fiber, with respective indices of the core and of the cladding, $n_{co} = 1.458$ and $n_{cl} = 1.453$. The transverse shape of the core is a truncated disk (see Fig. 1) invariant along the fiber.

Since we are dealing with a case of weak guidance $[(n_{co} - n_{cl})/n_{cl} \ll 1]$, it is expected that one can construct modes whose transverse field is essentially polarized in one direction. Indeed, in weakly guiding waveguides, though the index nonuniformity is essential to ensure total internal reflection, one may neglect it as far as polarization effects are concerned [17]. In spite of the edges of the transverse section, we checked that the linear polarization of light issued from our laser is indeed fairly well preserved throughout the fiber. We therefore will use the scalar approximation in the following theoretical approach.

A. Modal decomposition

We denote by z the position along the axis of the fiber and by r the position in the transverse plane. Using the translational invariance $n(r,z) = n(r)$, the three-dimensional (3D) Helmholtz stationary equation

$$(\Delta + \partial_{zz})\psi(r,z) + n^2(r)k_0^2\psi(r,z) = 0, \qquad (1)$$

where Δ is the transverse Laplacian, can be reduced to

$$\Delta\phi(r;\beta) + [n^2(r)k_0^2 - \beta^2]\phi(r;\beta) = 0, \qquad (2)$$

where $k_0 = 2\pi/\lambda$ (λ is the vacuum wavelength of the source) and

$$\psi(r,z) = \int d\beta\, \phi(r;\beta)e^{i\beta z}. \qquad (3)$$

For $\beta_{cl}^2 \equiv n_{cl}^2 k_0^2 \leqslant \beta^2 \leqslant \beta_{co}^2 \equiv n_{co}^2 k_0^2$, Eq. (2) is solved at discrete values, β_n, called the propagation constants of the guided modes. This eigenvalue problem can be written in a form

$$\left[-\frac{1}{2}\Delta + \frac{\beta_{co}^2 - n^2(r)k_0^2}{2} \right]\phi = \frac{\beta_{co}^2 - \beta^2}{2}\phi, \qquad (4)$$

which, by writing $V(r) = [\beta_{co}^2 - n^2(r)k_0^2]/2$, emphasizes the formal equivalence between Eq. (2) and a stationary Schrödinger equation

$$\left[-\frac{1}{2}\Delta + V(r) \right]\phi = E\phi. \qquad (5)$$

The *eigenenergy* E takes on discrete values E_n, related to the β_n's through

$$\beta_n^2 = \beta_{co}^2 - 2E_n. \qquad (6)$$

Using the basis generated by the eigenmodes ϕ_n of the Schrödinger equation (5), the solution of Eq. (1) can be written as

$$\psi(r,z) = \sum_n c_n\phi_n(r)\exp(i\,\beta_n z)$$

$$= \sum_n c_n\phi_n(r)\exp(i\,\sqrt{\beta_{co}^2 - 2E_n}\,z), \qquad (7)$$

where the sum should generically include the continuum states (nonguided modes with imaginary β's).

Defining $E_n = \kappa_n^2/2$, to each mode can be associated an angle θ_n with respect to the z axis defined by $\tan\theta_n = \kappa_n/\beta_n$ (or, equivalently, by $\sin\theta_n = \kappa_n/\beta_{co}$). The cutoff angle for guided modes is given by $\sin\theta_{max} = \sqrt{1 - (n_{cl}/n_{co})^2}$ (around 5° with the values of the indices given above), which corresponds to the maximum value $\kappa_{max} = \sqrt{\beta_{co}^2 - \beta_{cl}^2}$. This value is related to the total number of guided modes [18]. Indeed, the number of allowed values β_n in the interval $[\beta, \beta_{co}]$ (for a given polarization) is given by the Thomas-Fermi formula, which, in our context, reads

$$N(\beta) = \frac{1}{2\pi}\int_{E>V} dr[E - V(r)] = \frac{1}{2\pi}\int_{core} dr\, \frac{n^2(r)k_0^2 - \beta^2}{2}$$

$$= \frac{S}{4\pi}(\beta_{co}^2 - \beta^2) = \frac{S\kappa^2}{4\pi}, \qquad (8)$$

where S is the area of the core. This expression yields the well-known formula [19] for a cylindrical fiber of radius a: $N = v^2/2$, with $v = ak_0(n_{co}^2 - n_{cl}^2)^{1/2}$, when allowing for both polarizations. In our exotic fiber, the total number of modes (with a given polarization) is approximately 1500.

B. The paraxial approximation

Many of the theoretical results in the field of wave chaos have been obtained in the quantum context [7,18]. Though the introduction of the quantum formalism is not theoretically indispensable, it is quite convenient to our purposes and is easily performed through the following transformation. Starting from Eq. (5), one can write a pseudo-time-dependent Schrödinger equation

$$i\beta_{co}\partial_z\varphi(\mathbf{r};z) = \left[-\tfrac{1}{2}\Delta + V(\mathbf{r})\right]\varphi(\mathbf{r};z) \qquad (9)$$

which can be viewed as an evolution equation along z. Any solution $\varphi(\mathbf{r};z)$ of the above equation can also be decomposed on the ϕ_n's,

$$\varphi(\mathbf{r};z) = \sum_n c_n\phi_n \exp\left(-i\frac{E_n}{\beta_{co}}z\right). \qquad (10)$$

Note that Eq. (9) corresponds to the paraxial (or parabolic) approximation performed on Eq. (1). Indeed, if one writes

$$\psi(\mathbf{r},z) = \zeta(\mathbf{r};z)e^{i\beta_{co}z}, \qquad (11)$$

Eq. (1) becomes

$$i\beta_{co}\partial_z\zeta(\mathbf{r};z) = \left[-\frac{1}{2}\Delta + \frac{\beta_{co}^2 - n^2(\mathbf{r})k_0^2}{2}\right]\zeta(\mathbf{r};z)$$
$$-\frac{1}{2}\partial_{zz}\zeta(\mathbf{r};z) \qquad (12)$$

which is equivalent to Eq. (9) insofar as one may neglect the second order z derivative of ζ (paraxial or slowly varying amplitude approximation):

$$|\partial_{zz}\zeta| \ll |\beta_{co}\partial_z\zeta|. \qquad (13)$$

This neglect amounts to approximate the exact solution (7) of Eq. (1) by

$$\varphi(\mathbf{r};z)e^{i\beta_{co}z} = \sum_n c_n\phi_n(\mathbf{r})\exp\left(i\frac{\beta_{co}^2 - E_n}{\beta_{co}}z\right). \qquad (14)$$

The validity of this approximation is easily established in our experimental context. Indeed, by comparison of Eqs. (7) and (14), corresponding terms of each sum are close if the difference between their phases remains much smaller than 2π, i.e.,

$$\delta\beta \hat{=} \beta_{co} - \frac{E_n}{\beta_{co}} - \sqrt{\beta_{co}^2 - 2E_n} \simeq \frac{1}{2}\beta_{co}\left(\frac{E_n}{\beta_{co}^2}\right)^2 \ll \frac{2\pi}{z}. \qquad (15)$$

Condition (15) leads to values of θ somewhat smaller than the cutoff angle θ_{max}, when allowing for the actual length of the fiber. Therefore, this condition amounts to restricting the sum in Eq. (14) to the first few hundreds of guided modes.

III. FROM RAYS TO WAVE

We now consider the geometrical limit of rays and propose to do so by deriving the eikonal equation in the paraxial approximation. This is technically much simpler than deriving the eikonal equation directly from the 3D Helmholtz equation without restricting the generality of the ensuing results [20]. We are then naturally led to investigate a problem of *chaotic billiards* [21,22]. Then we will address the implications of chaotic ray motion on the statistical spatial properties of guided modes.

A. Chaotic ray motion

Starting from the parabolic equation (9), if one substitutes

$$\varphi(\mathbf{r};z) = A(\mathbf{r};z)\exp[i\beta_{co}\mathcal{L}(\mathbf{r};z)], \qquad (16)$$

two equations are obtained,

$$-2\partial_z\mathcal{L} = (\boldsymbol{\nabla}\mathcal{L})^2 + \left(1 - \frac{n^2(\mathbf{r})}{n_{co}^2}\right) - \frac{1}{\beta_{co}^2}\frac{\Delta A}{A}, \qquad (17)$$

$$\partial_z(A^2) = -\boldsymbol{\nabla}\cdot(A^2\boldsymbol{\nabla}\mathcal{L}). \qquad (18)$$

Equation (18) is simply a conservation equation for the "density" A^2, with "current" $A^2\boldsymbol{\nabla}\mathcal{L}$, whereas Eq. (17) is not the eikonal equation since it allows for diffraction effects through the last term of the right-hand side. Indeed, the true eikonal equation, associated to geometrical optics, is obtained by neglecting $\beta_{co}^{-2}\Delta A/A$, consistently with condition (13). It therefore reads

$$-\partial_z\mathcal{L} = H(\mathbf{r},\boldsymbol{\nabla}\mathcal{L}), \qquad (19)$$

where

$$H(\mathbf{r},\mathbf{p}_\perp) = \frac{\mathbf{p}_\perp^2}{2} + \frac{1}{2}\left(1 - \frac{n^2(\mathbf{r})}{n_{co}^2}\right) \qquad (20)$$

is the Hamiltonian and $\mathbf{p}_\perp$ is the transverse momentum. The rays of the geometrical limit are the characteristic curves $(\mathbf{r}(z),\mathbf{p}_\perp(z))$ of the Hamilton-Jacobi equation and satisfy the Hamilton equations

$$\frac{d\mathbf{r}}{dz} = \frac{\partial H}{\partial\mathbf{p}_\perp}, \qquad (21)$$

$$\frac{d\mathbf{p}_\perp}{dz} = -\frac{\partial H}{\partial\mathbf{r}}. \qquad (22)$$

These equations are straightforwardly solved for our fiber. Indeed, inside the uniform core, H is reduced to its "kinetic" part, $\mathbf{p}_\perp^2/2$, which can be related to the angle θ defined above through $\mathbf{p}_\perp^2 = \sin^2\theta$. At the boundaries between core and cladding, if $\sin^2\theta < (1-n_{cl}^2/n_{co}^2)$, the ray is reflected back to the core. Between two consecutive specular reflections, the ray consists of a straight segment. We have thus reduced the initial wave problem to the dynamics of a point particle inside a domain with perfectly rigid walls: a billiard [23].
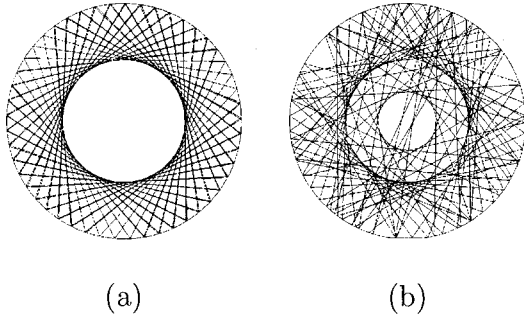
(a)   (b)

FIG. 2. Examples of a single ray trajectory after a propagation of 150 in units of the radius R: (a) inside a circular billiard, where a caustic is clearly observed; (b) inside a circular billiard cut by a small straight segment of length $10^{-2}R$. The caustic is destroyed due to the chaotic motion.

Here, the dynamics refers to the evolution along z and can be most easily visualized by projecting the ray trajectories onto the transverse plane. From now on, we will restrict our study of the motion to the two-dimensional (2D) projected motion.

Without going into technicalities, we wish now to illustrate the particular dynamics of chaotic billiards. Let us first recall the regular motion of rays in the billiard with the shape of a circle. Figure 2(a) shows a typical trajectory within such a billiard after a propagation length of 150 in units of the radius R. One can clearly observe the presence of a caustic. The latter encloses a region of space that this trajectory never visits (whatever the number of reflections). This kind of structure is destroyed in chaotic billiards. This is exemplified by considering the following modification of the previous billiard. A new shape is obtained by cutting a small straight segment of length $10^{-2}R$. Whereas the change of boundary is not visible in Fig. 2(b), its effect on the dynamics is dramatic: for the same initial conditions (position and direction), the formerly forbidden region is invaded after a finite number of reflections. In the theory of Hamiltonian chaos, it is shown that this effect stems from the *extreme sensitivity to initial conditions*, which appears for any nonvanishing size of the cut (excepted for a cut of length R, which corresponds to the semicircular billiard).

The qualification of chaos is more conveniently studied through a phase-space representation. A common representation in billiards consists in restricting the dynamics to the knowledge, at each impact, of the curvilinear abscissa, s, and of the sine of the angle of reflection, α, with respect to the inward boundary normal (see Fig. 3). Thus, at jth reflection, defining $\hat{\mathbf{t}}_j$ the unit vector tangent to the oriented boundary at abscissa s_j, and $\hat{\mathbf{n}}_j$ the inward normal unit vector, the transverse momentum reads $\boldsymbol{p}_\perp = \hat{\mathbf{t}}_j \sin\theta \sin\alpha_j + \hat{\mathbf{n}}_j \sin\theta \cos\alpha_j$. The same trajectories as in Fig. 2 are shown in the phase space $(s, \sin\alpha)$ in Fig. 4: the regular motion is associated to the conservation of α in the circular billiard [Fig. 4(b)], while in the truncated billiard, which is chaotic, the whole phase space is eventually uniformly covered by almost any trajectory [Fig. 4(b) shows the trajectory after a finite number of bounces, i.e., at finite time]. It should be mentioned here that there exist particular trajectories which do not fit into this scheme, namely, the periodic orbits. These orbits are
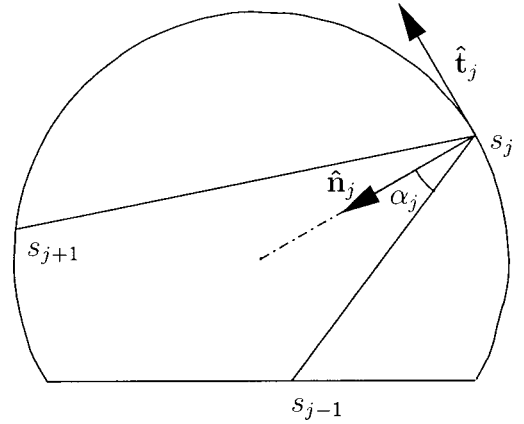

FIG. 3. Representation of the dynamics in a billiard through the coordinates associated, at each rebound, to the curvilinear abscissa s along the boundary, and the sine of the angle of reflection α with respect to the inward boundary normal.

trajectories which close upon themselves in phase space (hence also in real space). For a chaotic system they must, of course, be unstable in the sense that any small initial deviation from it must diverge exponentially with time. To be complete, the proper way of evidencing chaos in billiards is by considering the behavior of a collection of initial conditions. In Fig. 5, this set is initially shown as a dark disk in the phase space associated to the geometry of our actual fiber. Rapidly (exponentially with the number of reflections) the initial conditions will spread over the whole surface. This behavior is precisely the sign of Hamiltonian chaos.
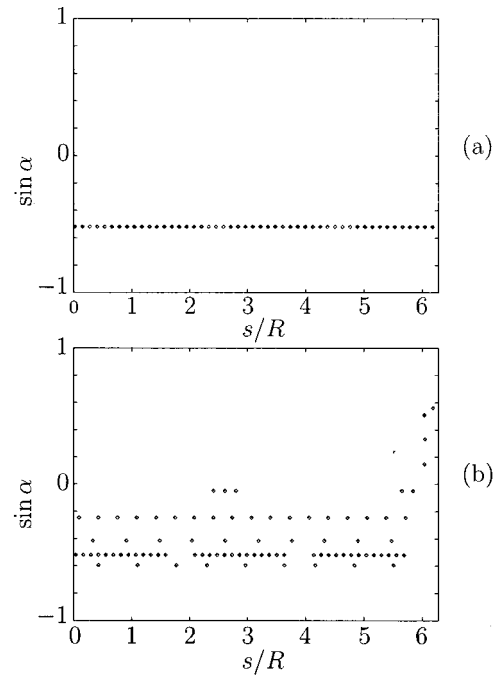

FIG. 4. Same trajectories as in Fig. 2 using the phase-space coordinates $(s, \sin\alpha)$ introduced in Fig. 3. (a) The regular motion in the circular billiard is associated to the conservation of α; (b) in the chaotic billiard, the whole phase space is asymptotically uniformly covered by almost any ray trajectory.
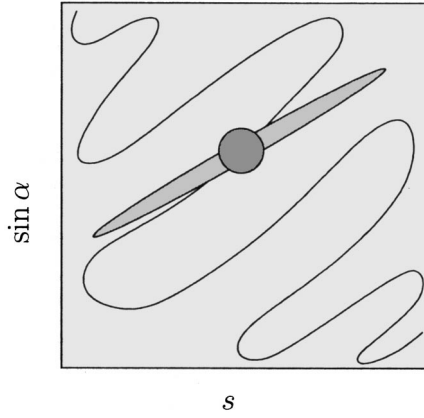
FIG. 5. Sketch of the typical evolution in phase space of a subset of initial conditions. Starting from an initial disk, subsequent stretching and folding are depicted at larger and larger times.

B. Gaussian statistics of ergodic guided modes

In the following, we will use the quantum terminology of semiclassical techniques to designate what is otherwise referred to as the geometrical theory of diffraction [24]. Thus, using the quantum analog of our optical waveguide, the geometrical limit of rays corresponds to the classical limit of a quantum problem. In our case, the small parameter for semiclassical expansions is $(\kappa L)^{-1}$, where $\kappa^2 = \beta_{co}^2 - \beta^2 = 2E$ and $L \sim \sqrt{S}$ is the typical size of the core [25], and ray trajectories have to be viewed as a genuine skeleton of wave motion [26]. In particular, the features of uniformity and isotropy resulting from the chaotic exploration of phase space by rays, as illustrated in the last section (Fig. 5), should be expected to govern, likewise, the statistical distribution of eigenmodes. The ergodicity of eigenmodes can be rigorously shown [27] and may be formally stated in writing down the *local density of states*,

$$\rho_0(\boldsymbol{r};\kappa) = \frac{\int d\boldsymbol{p}_\perp \, \delta(\kappa^2/2 - \beta_{co}^2 H(\boldsymbol{r},\boldsymbol{p}_\perp))}{\int d\boldsymbol{r}' d\boldsymbol{p}'_\perp \, \delta(\kappa^2/2 - \beta_{co}^2 H(\boldsymbol{r},\boldsymbol{p}_\perp))}$$

$$\equiv \lim_{\kappa L \to \infty} \langle |\phi(\boldsymbol{r})|^2 \rangle_\kappa, \qquad (23)$$

where the average reads

$$\langle |\phi(\boldsymbol{r})|^2 \rangle_\kappa = \frac{1}{N} \sum_n |\phi_n(\boldsymbol{r})|^2, \qquad (24)$$

the sum running over N eigenmodes centered around $E = \kappa^2/2$. This average is meaningful provided that the energy interval is large enough to ensure a large value of N, but small enough for the density of states to be approximately constant within this interval [28]. In practice, an average over a few modes is adequate, and the ergodic behavior can even become a generic feature of individual eigenmodes when $(\kappa L)^{-1}$ tends to zero. In Fig. 6, the squared amplitude of such an ergodic mode is shown. It has been obtained by numerically solving
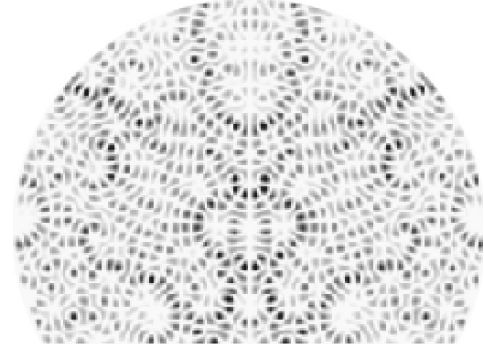

FIG. 6. A typical *ergodic* eigenmode (squared amplitude), solution of Eq. (25) with Dirichlet boundary conditions, in the truncated chaotic billiard with $\kappa R = 87.89$. Apart from the obvious symmetry, such an eigenmode can be viewed as a superposition of plane waves at a given κ with random phases and directions.

$$(\Delta + \kappa^2)\phi = 0 \quad \text{inside the core}$$

$$\phi = 0 \quad \text{on the boundary.} \qquad (25)$$

The above eigenvalue problem (with Dirichlet conditions) is a good approximation of Eq. (4) for low-lying guided modes. Nevertheless, the following qualitative arguments concerning the statistics of eigenmodes do not rely on this approximation. In Sec. IV, to analyze our experimental results, we will not use it. In Fig. 6, $\kappa = 87.89$ (in units of inverse radius of the billiard). This figure illustrates the fact that a typical eigenmode can be viewed as a random superposition of 2D plane waves of different phases and directions but with the same wave number κ [29].

If one views a typical specklelike guided mode locally as the superposition of plane waves with random directions, it may be shown that the field autocorrelation function

$$C_\phi(\boldsymbol{r},\boldsymbol{r}_0;\kappa) = \langle \phi^\star(\boldsymbol{r} - \tfrac{1}{2}\boldsymbol{r}_0)\phi(\boldsymbol{r} + \tfrac{1}{2}\boldsymbol{r}_0) \rangle_\kappa, \qquad (26)$$

where $\langle \cdots \rangle_\kappa$ is to be understood as an ensemble (energy) average in the asymptotic limit $\kappa L \gg 1$, has the expected value [30,31] [following the microcanonical result (23)]

$$C_\phi(\boldsymbol{r},\boldsymbol{r}_0;\kappa)$$

$$= \frac{\int d\boldsymbol{p}_\perp \exp[i\beta_{co}\,\boldsymbol{p}_\perp \cdot \boldsymbol{r}_0]\,\delta(\kappa^2/2 - \beta_{co}^2 H(\boldsymbol{r},\boldsymbol{p}_\perp))}{\int d\boldsymbol{r}'\,d\boldsymbol{p}_\perp\,\delta(\kappa^2/2 - \beta_{co}^2 H(\boldsymbol{r}',\boldsymbol{p}_\perp))}.$$

$$(27)$$

In the case of a 2D billiard, where $H(\boldsymbol{r},\boldsymbol{p}_\perp) = p_\perp^2/2$ in its interior, the Dirac δ function only fixes the norm of $\boldsymbol{p}_\perp$. Equation (27) thus amounts to the well-known result [31]

$$C_\phi(\boldsymbol{r},\boldsymbol{r}_0;\kappa) = J_0(\kappa r_0), \qquad (28)$$

where $J_0(x)$ is the zero-order Bessel function and r_0 is the norm of $\boldsymbol{r}_0$. Using an ergodic hypothesis, the average in Eq. (26) can be replaced by a spatial average over the midpoint $\boldsymbol{r}$,

which, in practice, should be evaluated over a domain encompassing a sufficiently large number of oscillations [30].

In the asymptotic limit, a random superposition of plane waves with random uncorrelated phases is expected to yield a Gaussian random field. In the case of real eigenmodes, this implies that the probability $P(\phi)d\phi$ that the eigenfunction has a value between ϕ and $\phi+d\phi$ is given by

$$P(\phi)=\frac{1}{\sqrt{2\pi\langle\phi^2\rangle}}\exp\left(-\frac{\phi^2}{2\langle\phi^2\rangle}\right), \tag{29}$$

where $\langle\cdots\rangle$ denotes a spatial average on the surface of the fiber section [32]. One should note that a Gaussian distribution does not imply the stronger requirement (27). The result (29) is also recovered by random matrix theory (RMT) for the Gaussian orthogonal ensemble of real symmetric $N\times N$ matrices in the limit $N\rightarrow\infty$ [28]. Indeed, RMT leads to the so-called Porter-Thomas distribution for the squared eigenvector components. The latter distribution is obtained from Eq. (29) for the intensity $I=\phi^2$ and reads

$$P(I)=\frac{1}{\sqrt{2\pi I\langle I\rangle}}\exp\left(-\frac{I}{2\langle I\rangle}\right). \tag{30}$$

To check this behavior, we first numerically solve the propagation equation (25) with Dirichlet boundary conditions using a plane-wave decomposition method. This method [33] has allowed the calculation of the first 2000 eigenmodes of the D-shaped billiard. Because of Dirichlet boundary conditions, the eigenmodes are chosen to be real.

Using these calculated modes, we have evaluated the *radial* field autocorrelation function $C_\phi(r_0;\kappa)$,

$$C_\phi(r_0;\kappa)=\frac{1}{2\pi}\int_0^{2\pi}d\theta\,C_\phi(r_0;\kappa) \tag{31}$$

with θ the polar angle and where the field autocorrelation function $C_\phi(r_0;\kappa)$ is equivalent to Eq. (26) with a spatial average over r,

$$C_\phi(r_0;\kappa)=\langle\phi^\star(r-\tfrac{1}{2}r_0)\phi(r+\tfrac{1}{2}r_0)\rangle_r, \tag{32}$$

where the average $\langle\cdots\rangle_r$ reads $\int\int_{\mathcal{D}}\cdots dr/\int\int_{\mathcal{D}}|\phi(r)|^2\,dr$, with $\mathcal{D}$ the domain of integration.

In Fig. 7, we have represented one typical high-energy eigenmode (amplitude) of the D-shaped billiard for a value of κ equal to 87.89 in units of inverse radius R, its probability distribution and the corresponding radial field autocorrelation function following Eqs. (31) and (32). The assumption of a random superposition of plane waves is confirmed by the good agreement between the probability distribution $P(\phi)$ and the Gaussian distribution, as can be seen in Fig. 7(b). The radial autocorrelation function $C_\phi(r_0;\kappa)$ is compared to the expected zero-order Bessel function $J_0(\kappa r_0)$ for $\kappa R=87.89$. Note that the prediction (28) is perfectly verified. From the oscillatory nature of the autocorrelation function, one should define a correlation length deduced from the
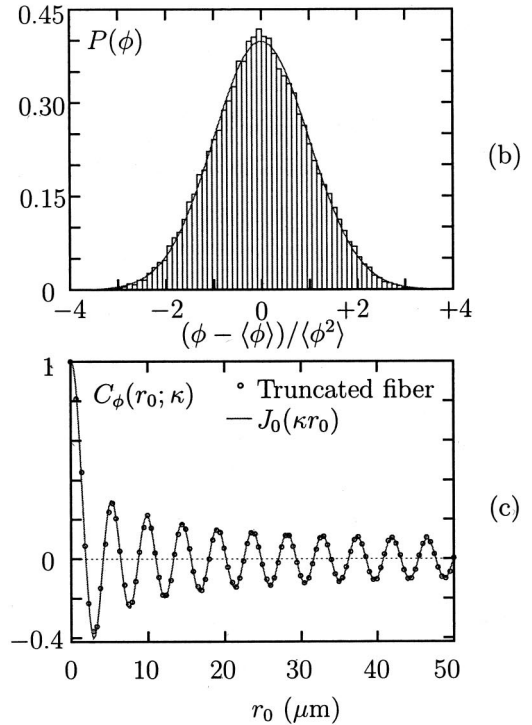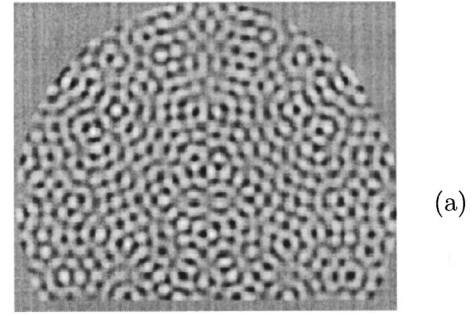

FIG. 7. (a) A high-energy eigenmode (amplitude) with $\kappa R = 87.89$ in the truncated chaotic billiard, (b) its associated probability distribution $P(\phi)$, compared to a Gaussian distribution (continuous line), and (c) the radial field autocorrelation function $C_\phi(r_0;\kappa)$.

quasiperiod of the autocorrelation function. This correlation length is related to the typical size of the speckle grain which is of the order of κ^{-1}.

In order to reveal the ergodic behavior of the chaotic eigenmodes of the D-shaped billiard, we have compared the previous results with those obtained for a typical high-energy mode of the circular billiard. For large values of the quantized number m associated to the number of zeros in the radial direction, there exists a simple relation between the couple of quantized numbers (l,m) associated to the regular eigenmode of the circular billiard and the value of κ given by [34]

$$\kappa\approx(l+2m)\frac{\pi}{2R},\quad m\gg1. \tag{33}$$

The resolution of Eq. (25) for the circular fiber yields solutions of the form
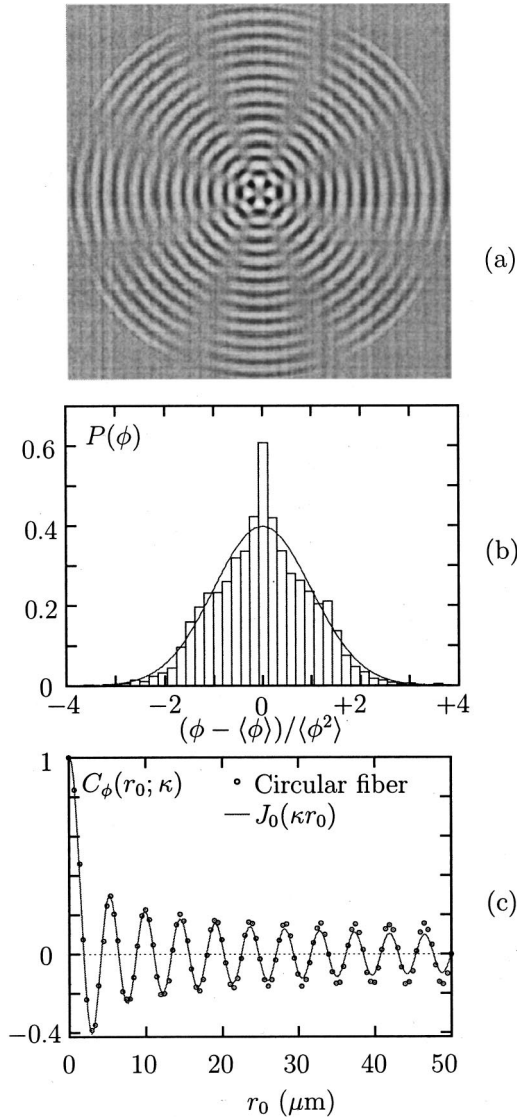
FIG. 8. (a) A high-energy eigenmode with $\kappa R = 87.0$ in the regular circular billiard, (b) its associated probability distribution $P(\phi)$, compared to a Gaussian distribution (continuous line), and (c) the radial field autocorrelation function $C_\phi(r_0; \kappa)$.

$$\phi_{l,m}(\mathbf{r}) = J_l(\kappa_m r) \times \begin{cases} \cos(l\vartheta) & \text{even solution} \\ \sin(l\vartheta) & \text{odd solution,} \end{cases} \quad (34)$$

where $J_l(\kappa_m R) = 0$ and ϑ is the angular variable in the circular coordinates. Using these relations, we have calculated one eigenmode of the circular billiard, for a value of $\kappa R \approx 87.0$, shown in Fig. 8(a). The associated probability [Fig. 8(b)] and the corresponding radial field autocorrelation function [Fig. 8(c)] deviate from the theoretical predictions (28) and (29) pertaining to ergodic modes. This is not surprising since the regular eigenmodes are obviously nonergodic. Indeed, in this context, a good test of ergodicity relies on the independence of the above statistical quantities on the spatial domain $\mathcal{D}$ introduced in Eq. (32) [30]. This domain defines the statistical sample used for the evaluation of the distribution probability. For the eigenmodes of the D-shaped fiber,
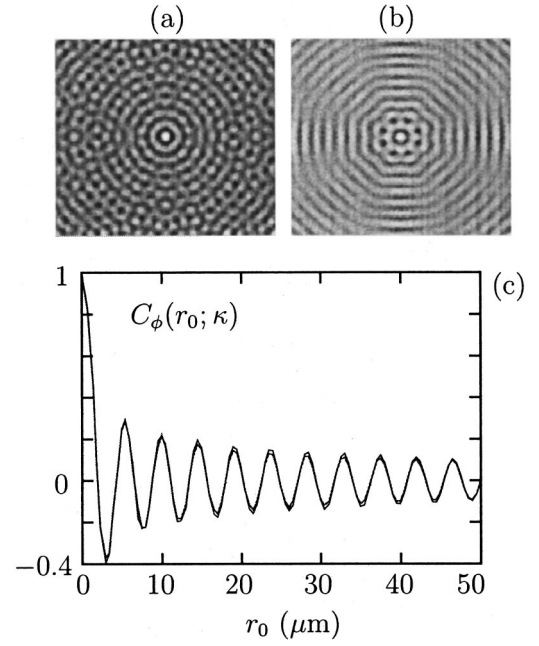

FIG. 9. Field autocorrelation functions for (a) an eigenmode of the truncated billiard, (b) an eigenmode of the circular billiard, and (c) their associated radial representations.

we have checked this independence. On the contrary, in the circular fiber, wide variations are observed from one sample to another. Surprisingly enough, for particular domains of this regular fiber, one can even observe that the behavior of the radial field autocorrelation function is very close to the zero-order Bessel function (Fig. 9). It does not necessarily follow from this result that the field autocorrelation function $C_\phi(\mathbf{r}_0; \kappa)$ (32) is isotropic, as implied by Berry's prediction (28) for ergodic eigenmodes. As an illustration, Fig. 9 displays the behavior of the field autocorrelation functions calculated for eigenmodes, with similar values of κ, of the D-shaped (a) and of the circular (b) fibers. Note that, while the *radial* autocorrelation functions for these two modes are nearly indistinguishable [Fig. 9(c)], only the ergodic eigenmode exhibits isotropic correlations.

C. Periodic orbit theory

As any prediction concerning average behaviors, the results presented in the previous section suffer rare but important exceptions. Indeed, inspecting Fig. 10(a), a clear deviation from ergodicity is seen, which is in fact associated to a particular periodic orbit (superimposed as a solid line). This intensity enhancement in the vicinity of a single periodic orbit (p.o.) is coined *scarring* [33,35]. This unexpected behavior has led the quantum chaos community to reconsider the semiclassical limit (23). They have established that the semiclassical skeleton of eigenmodes is built on all the periodic orbits of the system. Thus the one-to-one relationship shown in Fig. 10, between an eigenmode and a periodic orbit, has to be considered as an exception, since, as the number of p.o.'s proliferates exponentially with their lengths, eigenmodes must build upon many of them. The crucial role of p.o.'s had already been exemplified by the famous *trace*

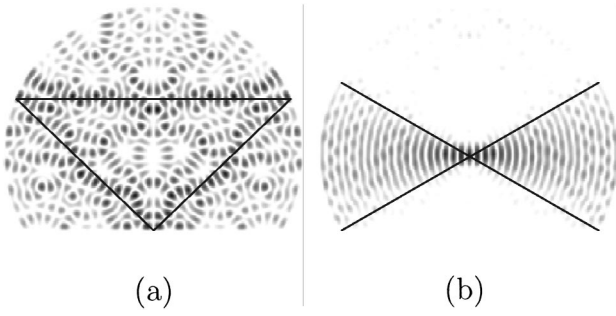(a)   (b)

FIG. 10. Examples of eigenmodes displaying an intensity enhancement in the vicinity of (a) an unstable periodic orbit (superimposed as a solid line) and (b) the continuous family of diameters (boundaries shown as solid lines).

formula [36], which establishes the semiclassical expression of the density of states $n(\kappa) = dN/d\kappa$,

$$n_{\mathrm{sc}}(\kappa) = n_0(\kappa) + \sum_p \ell_p w_p \exp(i\,\kappa\ell_p). \tag{35}$$

In the above equation, the sum is running over the periodic orbits, including multiple traversals, and ℓ_p is the total transverse length of orbit p. The quantity w_p encompasses a classical amplitude related to the stability of the orbit and a phase associated to caustics and reflections. The smooth part of the density (for the Dirichlet case) is given by the so-called Weyl formula [37]

$$n_0(\kappa) = \frac{S}{2\pi}\kappa - \frac{P}{4\pi}, \tag{36}$$

where P is the perimeter of the billiard and S is its surface. Note that the leading term of the above expression is directly obtained by differentiating Eq. (8). Considering the actual density of states $n(\kappa) = \Sigma_j \delta(\kappa - \kappa_j)$, Eq. (35) suggests that its Fourier transform provides a *length spectrum*, which dis-
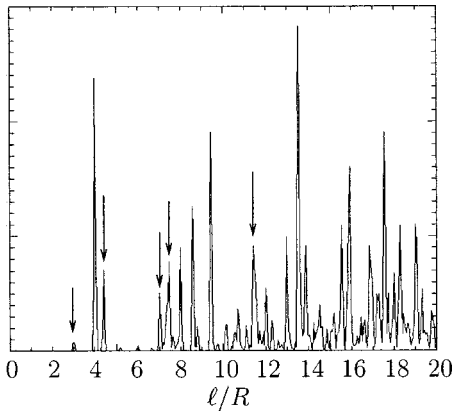

FIG. 11. The *length spectrum* or Fourier transform of the density of states $n(\kappa)$, for the eigenvalue problem (25) in the truncated chaotic billiard shown in Figs. 6 and 10. The *trace formula* permits us to show that the length spectrum should have peaks at the period lengths of the periodic orbits. Arrows indicate lengths corresponding to the periodic orbits shown in Fig. 12.

$\ell = 3$ $\ell = 4.4037$

$\ell = 7.0407$ $\ell = 7.3485$
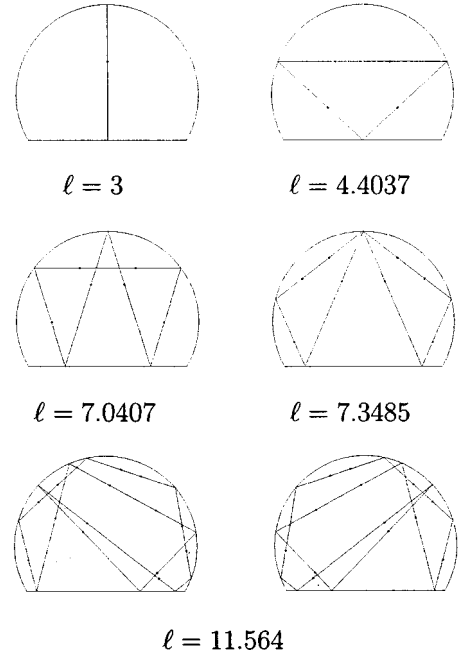
$\ell = 11.564$

FIG. 12. A few periodic orbits whose periods correspond to peaks of the length spectrum shown in Fig. 11.

plays peaks located at the lengths of the p.o.'s. In Fig. 11, we show the length spectrum of the above considered billiard. A few orbits among the shortest are indicated by arrows and are displayed in Fig. 12. Remark that the vast majority of periodic orbits contribute to the generic ergodic behavior described in the previous section. Interestingly enough, formula (35) allows us to recover many of the predictions of RMT [38]. Nonetheless, the least unstable periodic orbits or the continuous family of diameters which survived the truncation, and constitute marginally unstable periodic orbits, are responsible for the non-Gaussian statistics of the eigenmodes shown in Fig. 10.

IV. EXPERIMENTS

A. Fiber design

The fiber designed and fabricated in our lab for the experiment is now briefly described. Its transverse section is a truncated disk (see Fig. 1): a silica bar of 1-cm diameter is cut and polished and the fiber is pulled at a temperature low enough to avoid smoothing of the edges. This process ensures a small roughness (a few nanometers) of the planar surface. Moreover, since we only use lengths of the order of 10 cm, a high translational invariance is achieved (less than 3‰ error on the fiber diameter). The final dimensions are 120 μm for the diameter of the disk and 90 μm for the truncated diameter (Fig. 13). The cladding is composed of 40% of a black silicon (Rhodorsil RTV 1523 A) and 60% of transparent silicon (Rhodorsil RTV 1523 B). We use a black silicon cladding in order to avoid propagation of light in the cladding which could complicate the far-field intensity pattern. The indices are, respectively, $n_{\mathrm{co}} = 1.458$ in the core and $n_{\mathrm{cl}} = 1.453$ in the cladding. To prevent mode coupling due to bends or stresses, we keep the fiber straight by embedding it
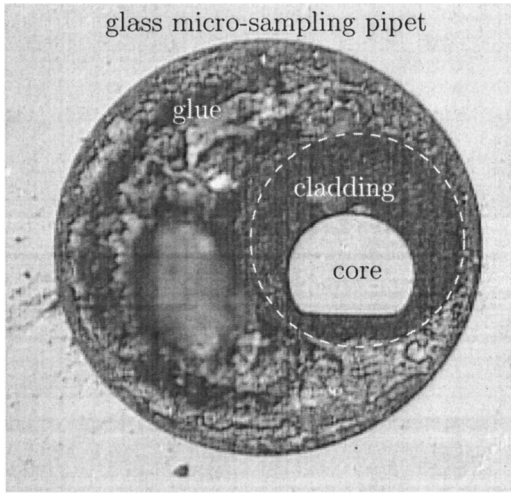
FIG. 13. Microscope observation of the transverse section of the fiber embedded in a glass microcapillary pipet.

in a glass microcapillary pipet. The set is kept together in a dural tube. A circular multimode fiber of 120-μm diameter with a black silicon cladding has been fabricated in the same way to compare spatial distributions of intensity for a chaotic and a regular billiardlike system.

B. Experimental setup

For our experiments, we use a He-Ne laser source ($\lambda = 632.8$ nm) with output power of 1 mW. The experimental setup is illustrated in Fig. 14. The laser beam of 1-mm diameter is first spatially filtered and expanded to obtain a 5-mm-diam beam. As a result, the final diameter is large compared with the 120-μm-diam fiber so that the laser beam may be viewed as a plane wave. We also performed another type of illumination by using a $\times 10$ microscope objective to focus the filtered and expanded beam on the fiber input.

The key parameter of the experiment is the incident direction of the beam given by the angle θ_0 between the beam and the fiber axis (Fig. 15). The incident angle of the beam on fiber input fixes the mean order of the excited modes by the way of the following simple relation:
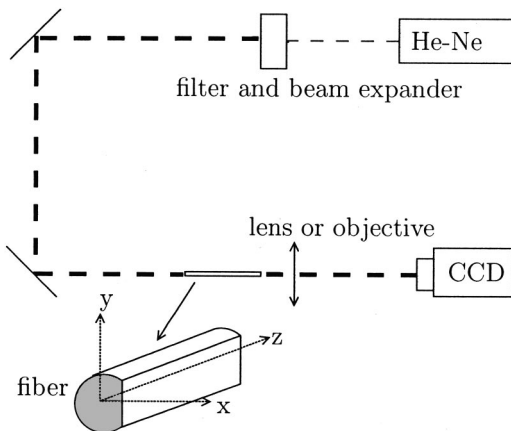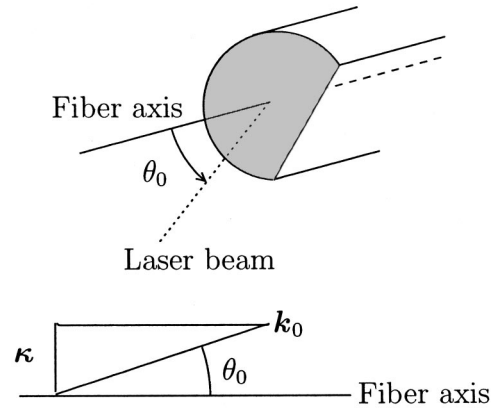

FIG. 14. Experimental setup.

FIG. 15. Relation between the incident angle on the fiber and the transverse wave vector κ.

$$\kappa_c = k_0 \sin \theta_0, \tag{37}$$

where $k_0 = 2\pi/\lambda$. Indeed, it should be kept in mind that, even with an ideal plane wave, the propagating wave in the fiber is essentially decomposed over a certain number of guided modes whose eigenvalues are centered on κ_c.

For the detection, we use a Sony CCD Camera of 398×288 pixel size. The CCD is used in its most sensitive regime (between 0.6 μm and 0.7 μm). At the output of the fiber, we detect either the near-field intensity or the far-field intensity. The near-field intensity is obtained by imaging the fiber output with a $\times 20$ microscope objective, whereas the far-field intensity is observed in the focal plane of a 2-cm-focal-length lens in the detection cell. Figure 16 shows typical near-field (a) and far-field (b) experimental intensity patterns at the fiber output for a quasi-plane-wave illumination.

C. Analysis of experimental results

Here, we propose an analysis of our observations based on the random Gaussian character of eigenmodes in the D-shaped fiber. The patterns of Fig. 16 are associated to a superposition of eigenmodes for a value of the transverse wave number $\kappa_c R$ equal to 36. This value is deduced from the mean radius of the ring in the far-field intensity observation. The far-field intensity $\tilde{I}(\kappa, \Theta)$ is essentially the squared modulus of the spatial Fourier transform $\mathcal{T}_F\{\psi(\boldsymbol{r})\}$ of the

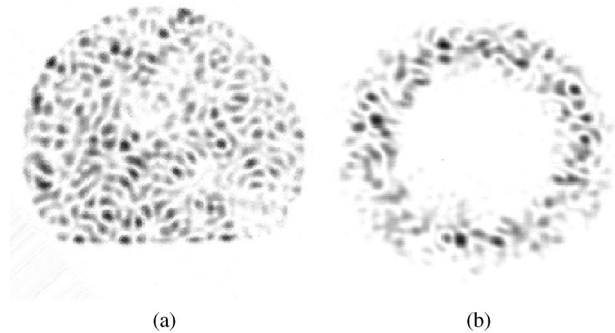(a)   (b)

FIG. 16. (a) Experimental near-field and (b) far-field intensity patterns for $\kappa_c R \approx 36.0$ for a quasi-plane-wave illumination.

field at the output of the fiber. The width of the ring in Fig. 16(b) gives an estimate of the number of excited modes. In practice, this number is evaluated by assuming a Gaussian shape for the radial envelope of the far-field intensity. Its full width at half-maximum fixes the κ interval around κ_c and yields 175 modes. The ring width we observe is more important than what we can theoretically expect from a plane-wave illumination. It is mainly due to the initial excitation: we do not have a perfect plane wave at the fiber input, so that several modes are excited.

Thus, the complex field $\psi(\mathbf{r},z)$ for a propagation length z reads

$$\psi(\mathbf{r},z) = \sum_{n=1}^{N} a_n \phi_n(\mathbf{r}) \exp(-i\beta_n z), \qquad (38)$$

where a_n is the weight of mode ϕ_n in the superposition, given by the projection of the initial condition on the eigenmodes basis $\{\phi_n\}$,

$$a_n = \int\int_S \phi_m^{\star}(\mathbf{r}) \psi(\mathbf{r},z=0) d\mathbf{r}/S \qquad (39)$$

with S the surface of the transverse section of the fiber and β_n the propagation constant associated to ϕ_n. The section of the fiber we study presents a symmetry axis. The eigenmodes basis is therefore naturally decomposed into even- and odd-parity modes which correspond to two independent spectra [18].

Here we use a concept inspired from quantum mechanics: In close analogy with the Heisenberg time [39], the *Heisenberg length* is defined as

$$z_H = 2\pi/\Delta\beta, \qquad (40)$$

where $\Delta\beta = 4\pi/(S\beta_{co})$ is the mean modal spacing for a given parity. Beyond this length, the guided modes can be considered as individually resolved leading to uncorrelated phases between modes in the decomposition (38). For a propagation length z longer than the Heisenberg length z_H, the products $a_n e^{-i\beta_n z}$ may be viewed as independent random variables. Indeed, this condition implies that the phase difference between two neighboring guided modes is greater than 2π. It is interesting to note that, in our system, the Heisenberg length

$$z_H = \frac{\beta_{co}S}{2} = n_{co}\frac{\pi S}{\lambda} \qquad (41)$$

may be viewed as an *effective* Rayleigh length [40]. For a Gaussian laser beam propagating out of the waist w_0, the Rayleigh length $z_R = \pi(w_0)^2/\lambda$ delineates the borderline between the Fresnel near-field and the Fraunhofer far-field regions. At distances large compared to the Rayleigh length, the full Fourier content of the laser beam is thus angularly resolved as are the individual modes fully resolved in our situation for distances large compared to the Heisenberg length.
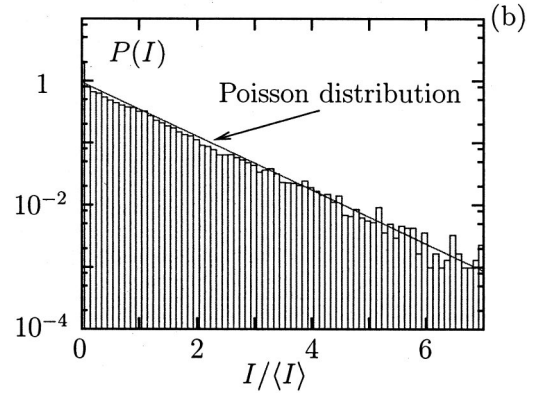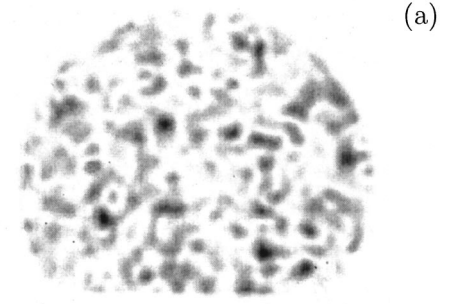

FIG. 17. (a) Mode superposition in the case of a focused excitation for the D-shaped fiber and (b) its intensity probability compared to the expected Poisson distribution.

Combining the expression (38) of the complex field with the previous assumption on the random behavior of the eigenmodes and of the terms $a_n \exp(-i\beta_n z)$, we deduce that the real and imaginary parts of the complex field $\psi(\mathbf{r},z)$ are themselves independent random Gaussian variables. This cannot be verified from the experimental results because we do not have experimental measurements of the complex field in the fiber. Nevertheless, using this Gaussian analysis, we can derive a prediction for the behavior of the probability distribution of the intensity and thus compare it to the results deduced from the measured intensity.

If we separate the intensity of the field $I = |\psi|^2$ using the real and imaginary part of the field assumed to be equivalent independent random Gaussian variables, we can derive the expression of the intensity probability $P(I)dI$ from the joint probability distribution. Its evaluation leads to the Poisson distribution

$$P(I) = \exp(-I/\langle I \rangle)/\langle I \rangle. \qquad (42)$$

Figure 17(b) illustrates the good agreement between the Poisson distribution issued from our Gaussian analysis and the intensity probability calculated from the measured near-field intensity of the superposition of modes presented in Fig. 17. The initial illumination is a focused beam with a $\times 10$ microscope objective. This experimental result agrees with our assumption on the Gaussian statistics of the eigenmodes of the truncated and chaotic fiber. A validation of this as-
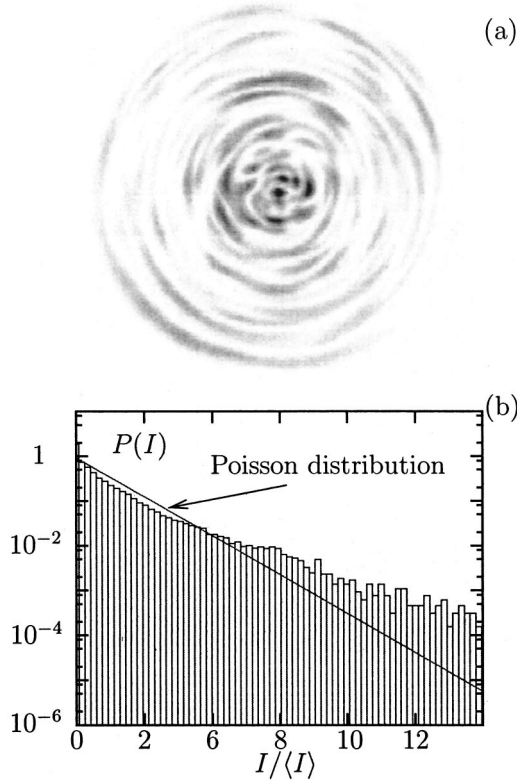
(a)

(b)

FIG. 18. (a) Mode superposition in the case of a focused excitation for the circular fiber and (b) its intensity probability compared to the Poisson distribution.
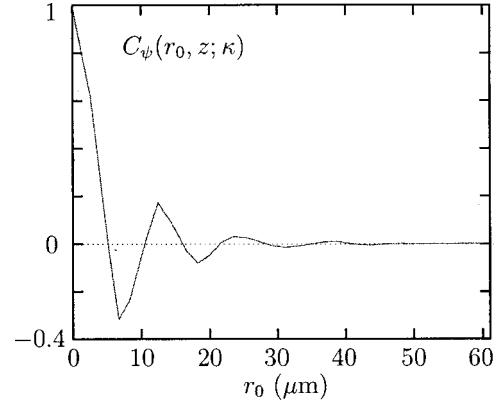

FIG. 19. The *radial* field autocorrelation function for $\kappa_c R \approx 30.0$ derived from the far-field intensity pattern of Fig. 16.

sumption will be provided by the investigations on the spatial autocorrelation functions which are much more sensitive to the nature of eigenmodes.

We now turn to compare this probability distribution to the one calculated for the near-field intensity pattern at the output of the circular fiber represented in Fig. 18(a) for a focused excitation by a $\times 10$ microscope objective. As seen before, we cannot use the Gaussian analysis to describe the behavior of the eigenmode of the circular fiber so that we do not expect a Poisson distribution for the intensity probability. In Fig. 18(b), we have plotted the intensity probability associated to the above intensity distribution. We can observe a large deviation from the Poisson distribution, thus confirming that the Gaussian analysis is only relevant for the description of chaotic systems.

We are now interested in evaluating the field autocorrelation function of a superposition of modes as measured in our experiment. Although the complex field at the fiber output cannot be measured directly, we deduce some of its properties from the far-field intensity. Indeed, the far-field intensity is proportional to the Fourier transform of the complex near field as the detector is placed in the focal plane of a lens.

The field autocorrelation function is deduced from the far-field intensity using the well-known Fourier transform relation

$$C_{\psi}(\boldsymbol{r}_0,z;\kappa_c) = \mathcal{T}_F^{-1}\{\tilde{I}(\kappa,\Theta)\}, \qquad (43)$$

where (κ,Θ) are the coordinates of the far-field space.

The autocorrelation function is thus obtained from the experimental observation by the way of a simple inverse Fourier transform performed on the far-field intensity. The *radial* function $C_{\psi}(r_0,z;\kappa_c)$ is then calculated from the vectorial function $C_{\psi}(\boldsymbol{r}_0,z;\kappa_c)$ using the angular integration (31) and is presented in Fig. 19. One should notice that the radial field autocorrelation still oscillates with a quasiperiod but quickly decreases as r_0 increases. It implies that long-range correlations within the complex field are reduced due to the superposition of several modes. As before, we use our Gaussian analysis to derive a prediction for the behavior of the field autocorrelation function for a superposition of modes. This analysis is original in the sense that we apply a modal approach to describe our experimental results.

The field autocorrelation function is defined as

$$C_{\psi}(\boldsymbol{r}_0,z;\kappa_c) = \langle \psi(\boldsymbol{r}+\boldsymbol{r}_0,z)\psi^{\star}(\boldsymbol{r},z)\rangle_{\boldsymbol{r}}. \qquad (44)$$

If one substitutes $\psi(\boldsymbol{r},z)$ by its expression (38), the field autocorrelation function reads

$$C_{\psi}(\boldsymbol{r}_0,z;\kappa_c) = \sum_{n,n'=1}^{N} \langle a_n a_n'^{\star}\phi_n(\boldsymbol{r}+\boldsymbol{r}_0)\phi_{n'}^{\star}(\boldsymbol{r})e^{-i\beta_n z}e^{i\beta_{n'}z}\rangle_{\boldsymbol{r}}$$

$$= \sum_{n=1}^{N} |a_n|^2\langle \phi_n(\boldsymbol{r}+\boldsymbol{r}_0)\phi_n^{\star}(\boldsymbol{r})\rangle_{\boldsymbol{r}}. \qquad (45)$$

The distinct eigenmodes are assumed to be statistically independent to derive the second expression. In relation (45) one can recognize the definition of the field autocorrelation function $C_{\phi}(\boldsymbol{r}_0;\kappa)$ [Eq. (32)] associated to an individual mode ϕ_n. Then, using the expression (28), we deduce the expression of the field autocorrelation function

$$C_{\psi}(\boldsymbol{r}_0,z;\kappa_c) = \sum_{n=1}^{N} |a_n|^2 J_0(\kappa_n r_0). \qquad (46)$$

As a consequence, the Gaussian analysis yields a field autocorrelation function written as a weighted sum of zero-order
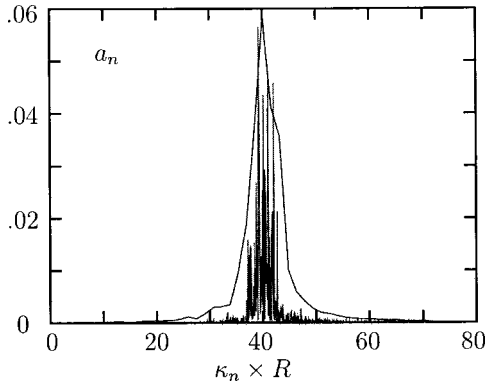
FIG. 20. Distribution of the coupling coefficients for a plane-wave illumination with $\kappa_0 R = 40.0$ and $\Theta = 17°$.

Bessel functions evaluated at each value of κ_n. Expression (46) thus includes the contribution of each eigenmode of the superposition (38) to the field correlations.

To calculate the right-hand side of Eq. (46), one needs to know the value of the square $|a_n|^2$ of the coupling coefficients which are defined by the condition of illumination (39). Experimentally, these terms cannot be perfectly evaluated. Indeed, only a smoothed version $b(\kappa)$ can be deduced from the measured far-field intensity

$$b(\kappa) = \frac{1}{2\pi}\int_0^{2\pi} \widetilde{I}(\kappa,\Theta)d\Theta, \qquad (47)$$

Θ being the angular variable in the spatial frequencies space (κ_x, κ_y).

To each eigenmode ϕ_n corresponds a ring pattern in the far field with mean radius κ_n. The width of each ring is ideally determined by the finite size of the section of the fiber and fixes the scale over which the weighted density $\Sigma|a_n|^2\delta(\kappa - \kappa_n)$ is smoothened to yield $b(k)$. Provided that the experimental resolution be sufficient, the evaluation of the $|a_n|^2$'s through $b(k)$ is thus intrinsically limited by diffraction. Nevertheless, we can numerically confirm the validity of our Gaussian analysis for the description of the field autocorrelation function using the calculated eigenmodes
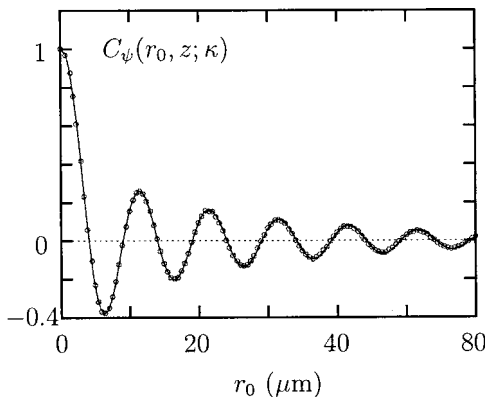

FIG. 21. Comparison between the experimental field autocorrelation function (circle) and the prediction derived from the Gaussian analysis (line).
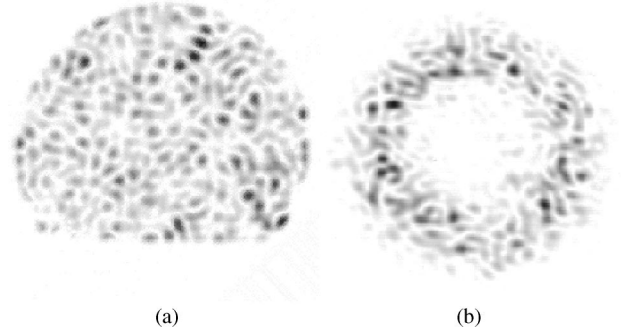

FIG. 22. (a) Near field and (b) far field at the output of a truncated fiber for $\kappa_c R \approx 29.0$.

(see Sec. III B). To do this, we project a plane wave $\exp(-i\kappa_0\cdot r)$ for a given value of κ_0 on the basis of the eigenmodes and we propagate this initial condition along the fiber by multiplying each eigenmode ϕ_n by the phase factor in the paraxial approximation $\exp(-i\beta_n z) \approx \exp[-i(E_n/\beta_{co})z]$. The expression of the field for a given length of propagation z is thus given by the relation

$$\psi(r,z) = \sum_{n=1}^{N} a_n\phi_n(r)\exp\left(-i\frac{E_n}{\beta_{co}}z\right). \qquad (48)$$

The coupling coefficients a_n are then derived from the projection of the initial condition $\exp(-i\kappa_0\cdot r)$ on the eigenmodes basis $\{\phi_n\}$ (39). In Fig. 20, we have plotted the distribution of the coupling coefficients associated to a plane-wave illumination with $\kappa_0 R = 40$ ($\kappa_0 = |\kappa_0|$). The corresponding smooth $b(\kappa)$ is also shown to exemplify the diffraction limit.

One can note that the distribution of the coupling coefficients is centered on the initial condition $\kappa_c R = \kappa_0 R = 40$. Using the coupling coefficients, we can evaluate the prediction (46) deduced from the Gaussian analysis. In Fig. 21, we have represented the field autocorrelation function calculated from the far-field intensity (43) compared with the evaluation of the expression (46). The agreement between the two curves is excellent, thus validating the choice of our modal Gaussian approach.

Even though the Gaussian analysis of the experimental field autocorrelation function is intrinsically spoiled by dif-
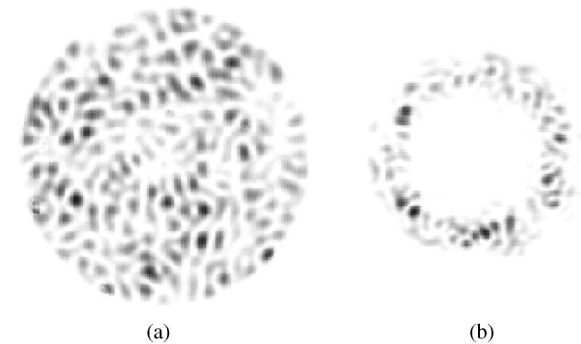

FIG. 23. (a) Near field and (b) far field at the output of a circular fiber for $\kappa_c R \approx 29.0$.
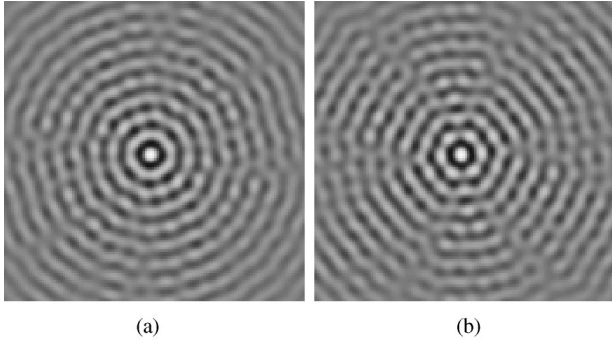
FIG. 24. Autocorrelation functions associated to filtered far fields (see text) for (a) the chaotic D-shaped fiber (far-field intensity patterns shown in Fig. 22) and (b) the regular circular fiber (Fig. 23). Note the hexagonal structure which is strongly marked near the origin in the nonergodic case.
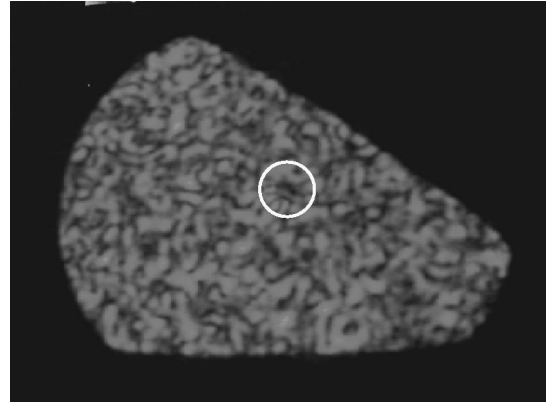

FIG. 25. Near-field intensity pattern at the output of a double-clad fiber with a doubly truncated inner cladding. The white circle delimits a chromium-doped core (IRCOM, Limoges).

fraction, one can nonetheless extract from it some information on the nature of the field. In particular, we can try to illustrate the essential difference in nature between the fields in the regular (circular) fiber and in the chaotic (truncated) fiber. We first consider the intensity patterns at the output of both fibers for a plane-wave illumination (Figs. 22 and 23). These intensity patterns correspond to the superposition of several modes around a central value of $\kappa_c R$ equal to 29. In order to extract the contribution to $C_\psi(\boldsymbol{r}_0, z; \kappa_c)$ of only a few eigenmodes, we perform a κ filtering by multiplying the far-field intensity pattern by a Gaussian ring. The width of the ring is fixed to $0.4/R$ (corresponding to the pixel size and approximately comprising nine modes) for both types of fiber (regular and chaotic) and its mean radius to $\kappa_c R \simeq 29$. We then calculate the autocorrelation functions associated to these filtered far-field intensity patterns by performing an inverse Fourier transform (43). The resulting autocorrelation functions are presented in Fig. 24. One can clearly see the isotropic behavior of the autocorrelation function associated to the field in the D-shaped fiber [Fig. 24(a)]. Indeed, this behavior is the signature of the ergodic nature of the chaotic eigenmodes of this truncated fiber. On the contrary, in the case of the circular fiber [Fig. 24(b)], privileged directions of high correlations mark the autocorrelation function. This nonisotropy results from the spatial distribution of the regular eigenmodes of the circular fiber which are characterized by a finite and well-defined number of zeros in the radial and angular coordinates.

So far we have only considered the ergodic nature of the chaotic eigenmodes. Deviations from this generic behavior are nevertheless observed that can be related to specific periodic ray motion associated to the short least unstable orbits of the system, leading to the so-called scarring phenomenon. A *scarred* eigenmode displays intensity enhancement along short periodic orbits (see Sec. III). The spatial localization of light induces strong correlations for both field and intensity and the resulting autocorrelation function exhibits strong anisotropy [16].

V. APPLICATION TO DOUBLE-CLAD FIBER AMPLIFIERS

Since the first appearance of erbium-doped fiber amplifiers (EDFA) in 1987, a novel way of using optical fibers has

proven its relevance and efficiency in optical telecommunications [41]. These EDFA's are now commonly used to restore optical signals in long-haul optical links. As applications in this domain require more and more powerful signals, high pump power levels are consequently needed. Double-clad fibers permit us to couple high pump power into the doped core. In these fibers, the doped amplifying single-mode (for the wavelength of the signal to be amplified) core is embedded in a multimode (for the pump wavelength) inner cladding where the pump is injected. Amplification is achieved by a transfer of the pump power from the inner cladding into the core as it propagates along the fiber. By using an inner cladding with the shape of a chaotic billiard, one may optimize the overlap of the pump field with the core along the propagation, thus reducing the differential modal absorption of the pump generally observed in standard circular double-clad fibers. Indeed, in a regular circular fiber, the overlap of guided modes varies widely from one mode to the other, thus leading to fluctuating transfer rates from the inner cladding into the core between modes. On the contrary, for the ergodic modes of a chaotic fiber, the overlap with the core region is essentially a constant. In a recent paper [42], we have proposed a quantitative theory for such an optimized pump absorption and provided numerical results in fair agreement with the predictions of our theory. The latter essentially relies on the fact that ergodic motion ensures a maximal and constant overlap of the pump intensity with the doped absorbing core along the fiber. We have also shown that suppression of marginally stable orbits can significantly improve the absorption characteristics of such double-clad EDFA's. Experimental demonstration of pump absorption optimization in a doubly truncated double-clad fiber has been recently achieved [43]. As an illustration, we show in Fig. 25 the experimental near-field intensity pattern of a chromium-doped double-clad fiber obtained by Ph. Leproux, Ph. Roy, J.-M. Blondy, and D. Pagnoux of the Guided and Integrated Optics group from Institut de Recherche en Communications Optiques (IRCOM) Limoges, France.

VI. CONCLUSION

In conclusion, we have provided the first complete theoretical and experimental characterization of wave intensity in

a chaotic multimode optical fiber in terms of spatial statistics and correlations. We have been able to confirm the validity of a Gaussian analysis for the statistics of the wave pattern in the speckle regime. Special attention was paid to the near-field autocorrelation function, which is obtained through the measurement of the far-field intensity, thus giving a dual way of characterizing the amount of randomness in the propagated field pattern. Starting from the above experiment, further progress is envisaged along the following directions: selective excitation of modes and parametric correlations in the frequency domain through the use of tunable laser sources.

This original experiment in multimode optical fibers provides interesting prospects to the applications of wave chaos concepts to modern technology as recently exemplified in optical fiber amplifiers based on double-clad chaotic fibers [42]. Furthermore, multimode optical fibers have recently received renewed interest in the context of optical multiplexing in transmission systems [44]. The feasibility of such network applications strongly relies on a proper understanding of propagation of light in complex fibers. The present work aims to serve this objective.

[1] A.J. Lichtenberg and M.A. Lieberman, *Regular and Stochastic Motion* (Springer-Verlag, New York, 1983).

[2] *Chaos and Quantum Physics*, edited by M-J. Giannoni, A. Voros, and J. Zinn-Justin, Les Houches 89, Session LII (North-Holland, Amsterdam, 1991).

[3] A. Altland, C.R. Offer, and B.D. Simons, *Quantum Chaos: Lessons from Disordered Metals*, in *Supersymmetry and Trace Formulæ: Chaos and Disorder*, edited by I.V. Lerner, J.P. Keating, and D.E. Khmelnitskii (Kluwer Academic, New York, 1999).

[4] *Mesoscopic Quantum Physics*, edited by A. Akkermans, G. Montanbaux, J.-L. Pichard, and J. Zinn-Justin, Les Houches 94, Session LXI (North-Holland, Amsterdam, 1995).

[5] H.-J. Stöckmann, *Quantum Chaos: An Introduction* (Cambridge University Press, Cambridge, England, 1999).

[6] C.E. Porter, *Statistical Theories of Spectral Fluctuations* (Academic Press, New York, 1965).

[7] D. Delande, *Chaos in Atomic and Molecular Physics*, in *Chaos and Quantum Physics*, edited by M-J. Giannoni, A. Voros, and J. Zinn-Justin, Les Houches 89, Session LII (North-Holland, Amsterdam, 1991).

[8] P.B. Wilkinson, T.M. Fromhold, L. Eaves, F.W. Sheard, N. Miura, and T. Takamasu, Nature (London) **380**, 608 (1996); L.P. Kouwenhoven, C.M. Marcus, P.L. McEuen, S. Tarucha, R.M. Westervelt, and N.S. Wingreen, *Electron Transport in Quantum Dots*, in *Proceedings of the Summer School on Mesoscopic Electron Transport* (Kluwer, Dordrecht, 1997).

[9] C.F. Bharucha, J.C. Robinson, F.L. Moore, B. Sundaram, Q. Niu, and M.G. Raizen, Phys. Rev. E **60**, 3881 (1999); D.A. Steck, W.H. Oskay, and M.G. Raizen, Science **293**, 274 (2001); W.K. Hensinger, H. Häffner, A. Browaeys, N.R. Heckenberg, K. Helmerson, C. McKenzie, G.J. Milburn, W.D. Phillips, S.L. Rolston, H. Rubinsztein-Dunlop, and B. Upcroft, Nature (London) **412**, 52 (2001).

[10] A. Kudrolli, M.C. Abraham, and J.P. Gollub, Phys. Rev. E **63**, 026208 (2001).

[11] R.L. Weaver, J. Acoust. Soc. Am. **85**, 1005 (1989); R.L. Weaver and O.I. Lobkis, Phys. Rev. Lett. **84**, 4942 (2000).

[12] J. de Rosny, A. Tourin, and M. Fink, Phys. Rev. Lett. **84**, 1693 (2000).

[13] S. Sridhar, Phys. Rev. Lett. **67**, 785 (1991); C. Dembowski, H.-D. Gräf, A. Heine, R. Hofferbert, H. Rehfeld, and A. Richter, *ibid.* **84**, 867 (2000); J. Stein, and H.-J. Stöckmann, *ibid.* **68**, 2867 (1992).

[14] J.U. Nöckel and A.D. Stone, Nature (London) **385**, 45 (1997).

[15] J. Krug, Phys. Rev. Lett. **59**, 2133 (1987); R.E. Prange and S. Fishman, *ibid.* **63**, 704 (1989); B. Fischer and A. Rosen, Opt. Lett. **24**, 1463 (1999).

[16] V. Doya, O. Legrand, F. Mortessagne, and Ch. Miniatura, Phys. Rev. Lett. **88**, 014102 (2002).

[17] A.W. Snyder and J.D. Love, *Optical Waveguide Theory* (Chapman and Hall, London, 1983).

[18] O. Bohigas, *Random Matrices and Chaotic Dynamics*, in *Chaos and Quantum Physics*, edited by M-J. Giannoni, A. Voros, and J. Zinn-Justin, Les Houches 89, Session LII (North-Holland, Amsterdam, 1991).

[19] D. Gloge, Appl. Opt. **10**, 2252 (1971).

[20] S.S. Abdullaev, *Chaos and Dynamics of Rays in Waveguide Media* (Gordon and Breach Science Publishers, Amsterdam, 1993).

[21] L.A. Bunimovich, Commun. Math. Phys. **65**, 295 (1979).

[22] S. Ree and L.E. Reichl, Phys. Rev. E **60**, 1607 (1999).

[23] O. Bohigas, M.J. Giannoni, and Ch. Schmit, Phys. Rev. Lett. **52**, 1 (1984).

[24] J.B. Keller, J. Opt. Soc. Am. **52**, 116 (1962).

[25] The semiclassical limit $\kappa L \gg 1$ has to be consistent with the paraxial hypothesis which, for the fiber we use, amounts to $\kappa L \lesssim 50$.

[26] F. Mortessagne, O. Legrand, and D. Sornette, Europhys. Lett. **33**, 417 (1996).

[27] A. Voros, Lect. Notes Phys. **93**, 326 (1979).

[28] F. Haake, *Quantum Signatures of Chaos* (Springer-Verlag, Berlin Heidelberg, 1991).

[29] M.V. Berry, *Semiclassical mechanics of Regular and Irregular Motion*, in *Chaotic Behaviour of Deterministic Systems*, edited by R.H.G. Helleman and G. Ioss, Les Houches 82, Session XXXVI (North-Holland, Amsterdam, 1983).

[30] M. Srednicki and F. Stiernelof, J. Phys. A **29**, 5817 (1996).

[31] M.V. Berry, J. Phys. A **10**, 2083 (1977).

[32] J.W. Goodman, *Statistical Properties of Laser Speckle Pat-*

terns, in *Laser Speckle and Related Phenomena*, edited by C. Dainty, Topics in Applied Physics Vol. 9 (Springer, Berlin, 1984).

[33] E.J. Heller, *Wave Packet Dynamics and Quantum Chaology*, in *Chaos and Quantum Physics*, edited by M-J. Giannoni, A. Voros, and J. Zinn-Justin, Les Houches 89, Session LII (North-Holland, Amsterdam, 1991).

[34] B.E.A. Saleh and M.C. Teich, *Fundamentals of Photonics* (John Wiley & Sons, New York, 1991).

[35] E. Bogomolny, Physica D **31**, 169 (1988).

[36] M.C. Gutzwiller, *Chaos in Classical and Quantum Mechanics* (Springer-Verlag, New-York, 1990).

[37] R. Balian and C. Bloch, Ann. Phys. (N.Y.) **63**, 582 (1971).

[38] M.V. Berry, *Some Quantum-To-Classical Asymptotics*, in *Chaos and Quantum Physics*, edited by M-J. Giannoni, A.

Voros, and J. Zinn-Justin, Les Houches 89, Session LII (North-Holland, Amsterdam, 1991).

[39] D. Delande, *The Semiclassical Approach for Chaotic Systems*, in *Waves and Imaging through Complex Media*, edited by P. Sebbah (Kluwer Academic Publisher, Dordrecht, 2001).

[40] A.E. Siegman, *Lasers* (University Science Books, Mill Valley, 1986), p. 668.

[41] E. Desurvire, *Erbium Doped Fiber Amplifiers* (Wiley Interscience, New York, 1994).

[42] V. Doya, O. Legrand, and F. Mortessagne, Opt. Lett. **26**, 872 (2001).

[43] Ph. Leproux, Ph.D. dissertation, Université de Limoges, France, 2001.

[44] H.R. Stuart, Science **289**, 281 (2000).